

Quantum impurity with $\frac{2}{3}$ local moment in one-dimensional quantum wires: A numerical renormalization group study

P. A. Almeida ¹, M. A. Manya,² M. S. Figueira ², S. E. Ulloa ³, E. V. Anda ⁴, and G. B. Martins ^{1,*}

¹*Instituto de Física, Universidade Federal de Uberlândia, Uberlândia, Minas Gerais, 38400-902, Brazil*

²*Instituto de Física, Universidade Federal Fluminense, Av. Litorânea s/N, 24210-340, Niterói, RJ, Brazil*

³*Department of Physics and Astronomy and Nanoscale and Quantum Phenomena Institute, Ohio University, Athens, Ohio 45701-2979, USA*

⁴*Departamento de Física, Pontifícia Universidade Católica do Rio de Janeiro (PUC-Rio), Rio de Janeiro, Rio de Janeiro, 22453-900, Brazil*

 (Received 25 May 2023; revised 21 September 2023; accepted 8 December 2023; published 8 January 2024)

We study a Kondo state that is strongly influenced by its proximity to an $\omega^{-1/2}$ singularity in the metallic host density of states. This singularity occurs at the bottom of the band of a one-dimensional chain, for example. We first analyze the noninteracting system: A resonant state ε_d , located close to the band singularity, suffers a strong renormalization, such that a bound state (Dirac δ function) is created below the bottom of the band in addition to a resonance in the continuum. When ε_d is positioned right at the singularity, the spectral weight of the bound state is $\frac{2}{3}$, irrespective of its coupling to the conduction electrons. The interacting system is modeled using the single-impurity Anderson model, which is then solved using the numerical renormalization group method. We observe that the Hubbard interaction causes the bound state to suffer a series of transformations, including level splitting, transfer of spectral weight, appearance of a spectral discontinuity, changes in binding energy (the lowest state moves farther away from the bottom of the band), and development of a finite width. When ε_d is away from the singularity and in the intermediate valence regime, the impurity occupancy is lower. As ε_d moves closer to the singularity, the system partially recovers Kondo regime properties, i.e., higher occupancy and lower Kondo temperature T_K . The impurity thermodynamic properties show that the local-moment (LM) fixed point is also strongly affected by the existence of the bound state. When ε_d is close to the singularity, the LM fixed point becomes impervious to charge fluctuations (caused by bringing ε_d close to the Fermi energy), in contrast to the LM suppression that occurs when ε_d is away from the singularity. We also discuss an experimental implementation that shows similar results to the quantum wire if the metallic host of the impurity is an armchair graphene nanoribbon.

DOI: [10.1103/PhysRevB.109.045112](https://doi.org/10.1103/PhysRevB.109.045112)

I. INTRODUCTION

The Kondo effect [1] has been extensively studied, both theoretically [2] and experimentally [3,4], and it is considered one of the pillars of many-body physics [5]. It is simulated by a quantum impurity coupled to a noninteracting Fermi sea, through a model that may include charge fluctuations, resulting in the well-known single-impurity Anderson model (SIAM) [6], or through a model that accounts only for the strong-coupling fixed point, where just spin fluctuations are relevant [7]—the so-called Kondo model [8]. The numerical renormalization group (NRG) method was developed in the 1970s [2,9–11], and it can uniquely tackle the Kondo problem. To this day, it is among the most popular techniques to deal with this fascinating problem. The main properties of the Kondo state—the quenching of the impurity magnetic moment, universal temperature scaling, and existence of renormalization fixed points—are readily obtained when considering a featureless (flat) density of states (DOS) of the host around the Fermi energy E_F , where most of the important physics occurs. This may be called a traditional Kondo effect. Things become more interesting, possibly

including non-Fermi liquid physics [12], when the host DOS behaves like $\rho(\omega) = |\omega|^r$ at or near the Fermi energy. For $r > 0$, the DOS vanishes at $\omega = 0$, and the band is said to have a pseudogap. Many theoretical works have analyzed the Kondo model (no charge fluctuations) for bands presenting a pseudogap [12–21], while much less work has been devoted to the $r < 0$ case, i.e., when there is a divergent DOS (singularity) at the Fermi energy [12,22–24]. Even fewer works have discussed [25–30] how a singularity close to the Fermi energy, generating high particle-hole (PH) asymmetry, modifies the Kondo state. Authors of recent work [31] have discussed a Kondo state where the impurity orbital level is resonant with a singularity at the bottom of the band (a situation that occurs for a one-dimensional (1D) lattice, nanotubes [32], and nanoribbons [33]), while the Fermi energy is slightly above the singularity, with very interesting results.

In this paper, we revisit a situation like the last system [31], using the NRG method. To better understand the system here, we first study the noninteracting regime. In the Appendixes, we discuss in detail what happens when a noninteracting resonant level (RL), generically called an impurity, is placed near (or at) the $\omega^{-1/2}$ singularity that occurs naturally in a 1D quantum wire host [see Fig. 1(a) for an illustration]. We show that the noninteracting RL spectral function $\rho_{U=0}$ [green curve in Fig. 1(a)] exhibits a bound state below the bottom of the band

*Corresponding author: gbmartins@ufu.br

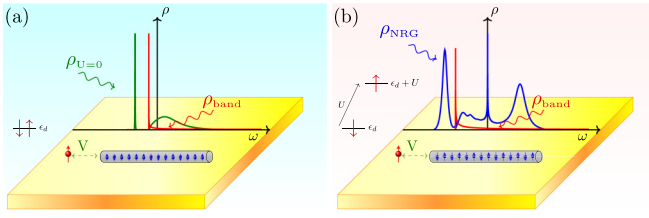


FIG. 1. Comparison of noninteracting and interacting results. (a) The red curve shows host density of states (DOS) with $\omega^{-1/2}$ singularity at the band bottom, while the green curve presents the DOS for a noninteracting impurity, showing a well-defined bound state below the continuum when ε_d is resonant with the band singularity. (b) Same as in (a) but now for an interacting impurity ($U \neq 0$). The bound state acquires a finite width, while a well-developed Kondo peak appears at the Fermi energy (see Appendix D for a critical discussion concerning the width of the bound state).

DOS ρ_{band} (red curve). The bound state has the properties of a Dirac δ function (see the Appendixes) and carries a spectral weight that depends on the coupling of the RL to the band and its distance to the singularity in ρ_{band} [visible as a sharp red peak in Fig. 1(a)]. Our results show a couple of interesting features of this deceptively simple noninteracting problem. First, there is a bound state even when the RL is positioned close to the center of the band. In that case, the bound state appears exactly at the edge of the band but carries negligible spectral weight, even for moderate coupling to the band (see discussion in Appendix C). Second, if the RL is positioned at the singularity, the bound state carries a spectral weight that is exactly $\frac{2}{3}$ [34], irrespective of the coupling strength of the RL to the band.

Once the Hubbard interaction U is turned on [see Fig. 1(b)], we find that the usual Kondo profile of the impurity spectral function [ρ_{NRG} , blue curve in Fig. 1(b)] is modified. Indeed, the singularity strongly distorts the lower Coulomb blockade peak (CBP) of the impurity, which is now composed of a broadened bound state and a series of peaks. In addition, the Kondo temperature and the impurity occupancy are strongly affected when ε_d is close to the band singularity. Both quantities tend to values closer to those fully in the Kondo regime (higher occupancy and lower T_K) even when the system is in an intermediate valence regime. This reentrant Kondo regime can also be observed at temperatures around the local-moment (LM) fixed point. Indeed, the magnetic susceptibility in the intermediate valence regime takes values like those in the Kondo regime at temperatures associated with the LM fixed point. This behavior, also visible in the NRG energy flow, is clearly associated with the existence of the bound state. We present NRG results and analysis to explore these interesting regimes in detail below.

The paper is organized as follows: In Sec. II, we present the Hamiltonian for the system to be analyzed, while Sec. III presents the NRG results. This section is divided into three parts: Sec. III A presents the dependence of the impurity spectral function (and charge occupancy) on the proximity of the impurity orbital level to the singularity at the bottom of the band. Section III B tracks how the bound state present in the noninteracting problem ($U = 0$) is affected by the

introduction of correlations (finite U). In Sec. III C, we analyze the impurity susceptibility as well as the impurity entropy and verify that the correlated states caused by the presence of the singularity have a strong influence on the impurity properties close to the LM fixed point. The thermodynamic results are interpreted through an analysis of the NRG energy flow. Section IV presents results for an experimentally accessible system, where these effects could be observed, viz., an $N = 3$ armchair graphene nanoribbon (AGNR). This system has two singularities, at the bottom of the conduction and valence bands, that have an $\omega^{-1/2}$ dependence, equal to that in a quantum wire system. Section V presents a discussion of the results and our conclusions. Finally, as mentioned above, in Appendixes A–C, we analyze in detail the noninteracting system when the RL is close to the singularity, while in Appendix D, we study the interacting (NRG) impurity spectral function to ascertain that the results in Sec. III A do not contain numerical artifacts.

II. MODEL AND HAMILTONIAN

In the following, we analyze the Kondo effect of an impurity coupled to a 1D quantum wire. We start with the quantum wire Hamiltonian:

$$H_{\text{wire}} = \sum_{k,\sigma} (-2t \cos k - \mu) c_{k\sigma}^\dagger c_{k\sigma}, \quad (1)$$

where $c_{k\sigma}^\dagger$ creates an electron with wave vector k and spin $\sigma = \uparrow, \downarrow$, while $t = 0.5$ is the nearest-neighbor hopping in the tight-binding chain (thus, $D = 1$, the half bandwidth, is our unit of energy), and μ is the chemical potential. The Fermi energy, for different values of μ , is always set at zero ($E_F = 0$).

To study the Kondo state in this system, the wire is coupled to an Anderson impurity, which is modeled as

$$H_{\text{imp}} = \sum_{\sigma} \varepsilon_d n_{\sigma} + U n_{\uparrow} n_{\downarrow}, \quad (2)$$

where d_{σ}^\dagger (d_{σ}) creates (annihilates) an electron with orbital energy ε_d and spin $\sigma = \uparrow, \downarrow$, $n_{\sigma} = d_{\sigma}^\dagger d_{\sigma}$, and U represents the Coulomb repulsion. The hybridization between the impurity and the conduction electrons is given by

$$H_{\text{hyb}} = \sum_{k\sigma} (V_k d_{\sigma}^\dagger c_{k\sigma} + \text{H.c.}), \quad (3)$$

where we consider the case of $V_k \equiv V$. The parameter $\Gamma = \pi V^2 \rho_{\text{band}}(E_F)$ determines the strength of the coupling of the impurity to the bath, where $\rho_{\text{band}}(E_F)$ is the DOS of the host at the Fermi energy. To solve this problem, we use the well-known NRG Ljubljana open source code [35]. For most of the calculations, we have used the discretization parameter $\Lambda = 2.0$ and kept at least 5000 states at each iteration. We also employ the so-called z trick [36] (with $z = 0.0625, 0.125, \dots$, and 1.0 , i.e., $N_z = 16$) to remove oscillations (artifacts) in the physical quantities. The Kondo temperature was obtained through Wilson's criterion [1], namely, the temperature for which the impurity susceptibility multiplied by the temperature reaches 0.07. The thermodynamic quantities were calculated using the traditional single-shell approximation,

while the dynamical quantities (spectral function) were calculated using the density matrix NRG approximation [37]. Finally, the single-particle calculations in the main text (and in Appendix D) have used an imaginary part $\eta = 10^{-6}$ to regularize the Green's function.

III. NRG RESULTS

A. Singularity effect on the impurity spectral function and charge occupancy

As described in the literature [25–30], the Kondo state for Anderson-type systems [6] and highly asymmetric DOS (such as when the Fermi energy E_F is close to a Van Hove singularity) strongly depends on model parameters. Indeed, our detailed analysis of the Kondo state for E_F close to the 1D band singularity [38] indicates that the impurity spectral function, impurity charge occupancy, and thermodynamic properties are very sensitive to the interplay between ε_d , U , V , and E_F . In other words, small changes in the parameters, like the position of E_F in relation to the singularity, strongly affect the Kondo state.

To reveal the most interesting aspects of the Kondo state when ε_d is at the singularity (and E_F is close to the bottom of the band), we will contrast it to the Kondo state obtained when E_F is exactly in the middle of the band ($\mu = 0$), keeping all the other parameters equal. We take $\varepsilon_d = -U/2$; thus, for $\mu = 0$, the system is in the PH-symmetric (PHS) point. These results are shown in Fig. 2. Panels (a) and (b) show the impurity spectral function (green curve for the noninteracting case $\rho_{U=0}$ and blue curve for the interacting case ρ_{NRG}) for $\mu = 0$ and -0.995 , respectively. The (red) dashed curves are the band DOS ρ_{band} . Note that all DOS results are normalized so that their integrals over ω are 1. The parameters, kept fixed for both calculations, are $\varepsilon_d = -0.005$, $U = 0.01$, and $\Gamma = 6.6667 \times 10^{-4}$ (thus $U/\Gamma = 15$). We have used V values for both calculations ($V = 0.026$ and 0.0082 , for panels (a) and (b), respectively) such that Γ does not vary. The only change from one calculation to the other is the PH asymmetry around E_F : no asymmetry in panel (a) and very strong asymmetry in panel (b). Comparison of the ρ_{NRG} results (blue curves) in panels (a) and (b) shows how strongly the singularity affects the impurity spectral density [39]. Indeed, from a traditional PHS Kondo peak at $\mu = 0$ [panel (a), blue curve], we move to a very rich impurity DOS when ε_d is at the singularity, showing a series of peaks around the Fermi energy ($E_F = 0.0$). The rightmost peak in ρ_{NRG} (the upper CBP), farthest from the singularity, is the least affected, while the Kondo peak (around $\omega = 0.0$) acquires slight asymmetry. Notice that the RL results (green curve, $\rho_{U=0}$) show that the singularity splits the noninteracting DOS into a Dirac δ -like bound state (below the bottom of the band) and a broad peak starting at the bottom of the band. As it turns out, this last peak becomes a superposition of three peaks in the continuum, while the bound state splits into two features below the band. One is very sharp, located at the band edge, and has very small spectral weight. The other, containing most of the spectral weight, is shifted to lower energy than the original bound state and acquires a sizable finite width [40]. Thus, the interplay between the singularity and correlations results in very complex spectral behavior. This will be further analyzed in the next subsection, Sec. III B.

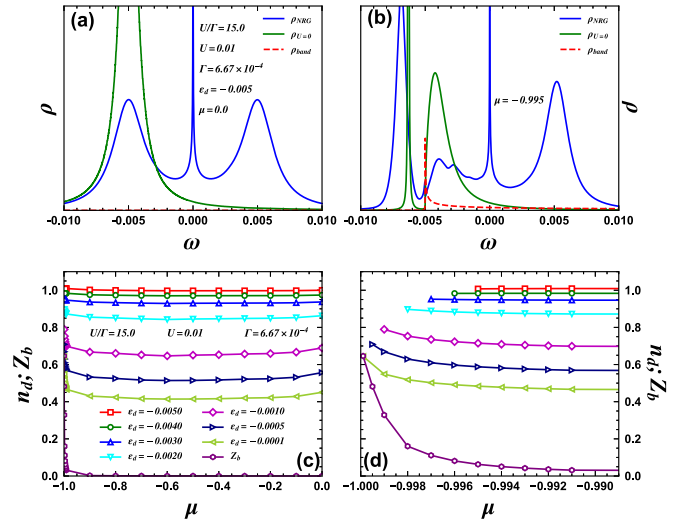


FIG. 2. Density of states (DOS) comparison and spectral weights for $U = 0$ and 0.01 . (a) Impurity DOS for $U = 0$ ($\rho_{U=0}$, green curve) and for $U/\Gamma = 15$ (ρ_{NRG} , blue curve) for $\mu = 0$ (when E_F is at the center of the band, $\omega = 0.0$), $U = 0.01$ and $\varepsilon_d = -U/2 = -0.005$ (notice dashed red curve close to the horizontal axis, showing the band DOS, ρ_{band}). (b) Same as in (a) but now with E_F very close to the singularity at the bottom of the band (depicted by the dashed red curve, ρ_{band}), $\mu = -0.995$, $\varepsilon_d = -0.005$ (right at the singularity). In (a) and (b), the Γ value is the same for finite and vanishing U . (c) Finite $U = 0.01$ results for the evolution of $n_d = \langle n_{d\uparrow} + n_{d\downarrow} \rangle$ as E_F moves from the center of the band ($\mu = 0$, right side) to very near the singularity ($\mu = -1.0 - \varepsilon_d$, left side), for different values of ε_d (the leftmost value of μ places the resonant level (RL) exactly at the singularity). The lowest (purple hexagons) curve with hexagons shows the bound state spectral weight Z_b (see the Appendixes), for $U = 0$ and $\varepsilon_d = -0.0001$. (d) Zoom of the left side of (c) highlighting the abrupt increase in n_d . The lowest value of the chemical potential is $\mu = -1.0 - \varepsilon_d$; thus, the curves above do not cover the same μ interval.

Figure 2(c) shows how the impurity occupancy $n_d = \langle n_{d\uparrow} + n_{d\downarrow} \rangle$ (for $U = 0.01$ and $U/\Gamma = 15$) varies when the Fermi energy moves from the center of the band ($\mu = 0$) to close to the bottom of the band ($\mu = -1.0 - \varepsilon_d$), for different values of ε_d ($-0.005 \leq \varepsilon_d \leq -0.0001$). Figure 2(d) shows a zoom of the results in panel (c) close to the lowest values of μ . Notice that the red-squares curve at the top for $\varepsilon_d = -0.005$ is at the PHS point for $\mu = 0$, and the occupancy is pinned at $n_d = 1$ even as μ moves away from PHS. As expected, the average value of n_d decreases (from $n_d \approx 1.0$ to 0.45) as ε_d increases, from $\varepsilon_d = -U/2 = -0.005$ (red squares) to very close to the Fermi energy $\varepsilon_d = -0.0001$ (light green left triangles), moving the system from deep into the Kondo regime to an intermediate valence regime, even for $\mu = 0$. However, as the Fermi energy approaches the bottom of the band ($\mu \approx -1.0 - \varepsilon_d$), n_d increases abruptly, with a faster rate the closer ε_d is to zero.

The variation of the bound state spectral weight Z_b [41] [purple hexagons curve in Fig. 2(c)] with μ , for the noninteracting case, indicates that once the system moves to the intermediate valence regime (larger values of ε_d), the presence of the bound state below the bottom of the band, with

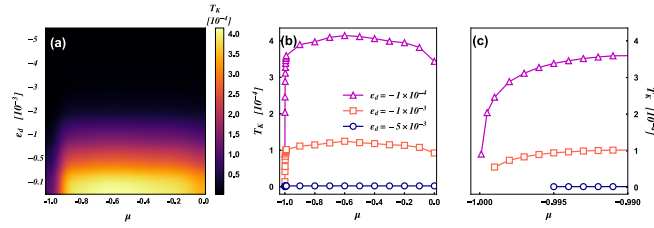


FIG. 3. (a) Color map of the Kondo temperature T_K for all the points in Fig. 2(c). The sudden drop of T_K at the bottom left corner indicates that the bound state near E_F moves the system back to the Kondo regime, which has a lower T_K than in the intermediate valence regime (bottom right corner). (b) Comparison of T_K vs μ results for $\varepsilon_d = -1 \times 10^{-4}$ (magenta triangles, intermediate valence regime), $\varepsilon_d = -1 \times 10^{-3}$ (orange squares, border between Kondo and intermediate valence regimes), and $\varepsilon_d = -5 \times 10^{-3}$ (blue circles, deep into Kondo regime). (c) Zoom of the results in (b) close to the bottom of the band.

stronger spectral weight, strongly increases the charging of the impurity. This effect is negligible if the system is well into the Kondo regime ($\varepsilon_d = -0.005$, red squares) or close to it ($\varepsilon_d \lesssim -0.003$).

As n_d tends to approach its Kondo value of $n_d \approx 1.0$, despite ε_d approaching the intermediate valence regime, close to the bottom of the band, it is reasonable to expect that the Kondo temperature T_K will be strongly affected. We expect T_K will tend to return to its Kondo value when we approach the bottom of the band in the intermediate valence regime. Indeed, this can be seen in Fig. 3(a), showing a color map of the Kondo temperature T_K for all the points in Fig. 2(c). Focusing on the right side of the figure ($\mu = 0$, E_F at the center of the band), we see the usual increase in T_K as we move from top to bottom (from the Kondo to the intermediate valence regime). However, looking at the bottom of the figure, moving from right to left (from center to bottom of the band), we see that T_K decreases abruptly as we approach the bottom of the band, tending back to its low Kondo-regime value. Figure 3(b) shows a comparison of results for T_K vs μ for different $\varepsilon_d = -1 \times 10^{-4}$ (magenta triangles, intermediate valence regime), $\varepsilon_d = -1 \times 10^{-3}$ (orange squares, border between Kondo and intermediate valence regimes), and $\varepsilon_d = -5 \times 10^{-3}$ (blue circles, Kondo regime), highlighting the sharp drop in T_K as μ approaches the singularity, when the system is in the intermediate valence regime (magenta triangles) or in a region in between Kondo and intermediate valence [42] (orange squares). This contrasts the stable behavior of T_K when the system is deep into the Kondo regime (blue circles). Figure 3(c) shows a zoom of the results close to the singularity. Indeed, the formation of the bound state close to the Fermi energy seems to bring the system back to a Kondo regime [43].

B. Evolution of the bound state with correlations

With the objective of understanding the origin of the split peaks around the singularity visible in Fig. 2(b), we present in Fig. 4 the evolution of the interacting impurity spectral function as U decreases, keeping $\Gamma = 8.334 \times 10^{-4}$, $\varepsilon_d = -U/2$, and varying μ so that, for all panels, ε_d is at the singularity

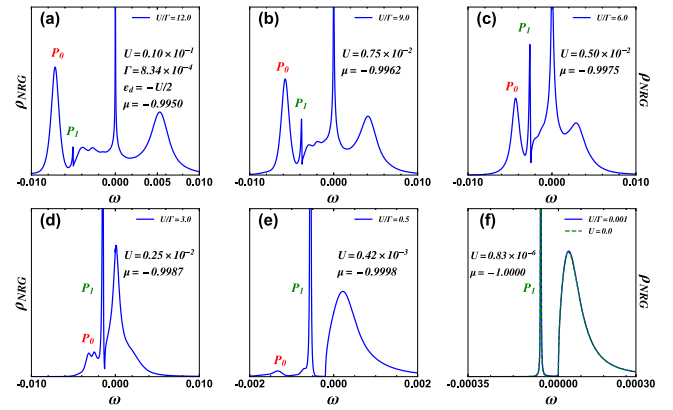


FIG. 4. Evolution of the interacting impurity spectral density ρ_{NRG} (blue curves), for $\Gamma = 8.34 \times 10^{-4}$, $\varepsilon_d = -U/2$, and $\mu = -1.0 - \varepsilon_d$, as U varies from (a) $U/\Gamma = 12$ to (f) 0.001. The value of μ places ε_d at the singularity in all panels. The dashed green curve in (f) is the noninteracting $\rho_{U=0}$ spectral function, showing excellent agreement with the $U \approx 0$ numerical renormalization group (NRG) result. The peaks P_0 and P_1 are associated with the bound state seen in $\rho_{U=0}$ (see text).

($\mu = -1 - \varepsilon_d$). Panels (a)–(f) show results for $U/\Gamma = 12.0$, 9.0, 6.0, 3.0, 0.5, and 0.001, respectively (as indicated in each panel). With decreasing U , the upper CBP moves to lower energy, eventually merging with a considerably broader Kondo peak [panel (c)], resulting from the system having entered an intermediate valence regime [43]. We now focus our attention on the two peaks below the bottom of the band, whose position and spectral weight can be followed more accurately [peaks P_0 and P_1]. For decreasing U/Γ , the leftmost peak P_0 transfers its spectral weight to peak P_1 , located at the bottom of the band. Indeed, for $U/\Gamma \lesssim 0.5$ [panel (e)], P_0 has transferred almost all of its spectral weight to P_1 , while in the interval $3 \lesssim U/\Gamma \lesssim 6$, peak P_0 splits into two peaks. For $U/\Gamma \approx 9.0$, P_1 detaches from the bottom of the band, moving away from it for smaller U , while its spectral weight increases at the expense of P_0 . Panel (f), for $U/\Gamma = 0.001$, has a comparison of the NRG (blue curve) and $U = 0$ results [44] (dashed green curve), showing that they are virtually the same. This demonstrates that the NRG spectral function results reproduce faithfully the evolution of the many-body processes that give origin to the split peaks around the singularity, deep into the Kondo regime [panel (a), $U/\Gamma = 12$].

We now analyze ρ_{NRG} in more detail in panels (a) and (b), where we still have strong correlations. In both panels, a well-formed Kondo peak and an upper CBP are clearly visible. For $U/\Gamma = 9$, at energies below the Kondo peak (but still inside the continuum), a structure with two features is clearly visible. For $U/\Gamma = 12$, the Kondo peak and the upper CBP are clearly consolidated, and further structure (a third smooth feature) emerges between the Kondo peak and the bottom of the band. In Appendix D, we show that all these features (including P_0 and P_1) are not NRG artifacts.

Figure 5 presents the spectral weight [panel (a)] and position [panel (b)], in relation to the bottom of the band, of peaks P_0 and P_1 for different values in the interval

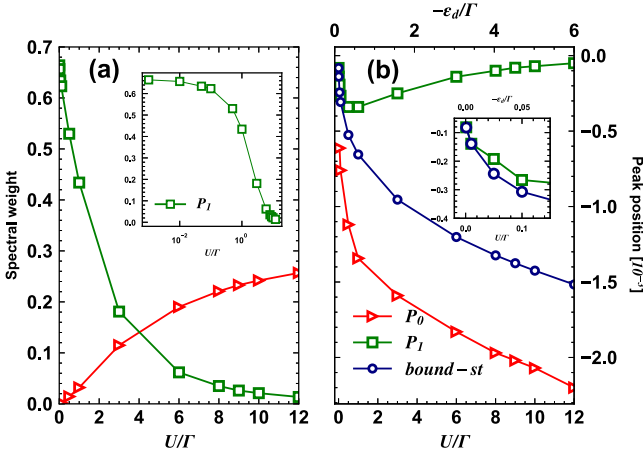


FIG. 5. (a) Spectral weight, as a function of U/Γ , for peak P_0 (red right triangles) and peak P_1 (green squares), as defined in the discussion of Fig. 4. The inset shows P_1 spectral weight in a log scale, highlighting the $\frac{2}{3}$ plateau for vanishing U . (b) Energy position, in relation to the bottom of the band, of P_0 (red right triangles), P_1 (green squares), and the noninteracting bound state (blue circles). The inset shows the exact agreement between P_1 and the bound-state positions for the smallest values of U . Note that the noninteracting ($U = 0$) bound-state results (blue circles) are dependent on $-\varepsilon_d/\Gamma$ (upper horizontal axes in the main panel and its inset), with $\varepsilon_d = -U/2$, where the U and V values are defined by the numerical renormalization group (NRG) results.

$0.001 \leq U/\Gamma \leq 12.0$. In panel (b), we also plot the position of the noninteracting bound state (blue circles), for $U = 0$ and the same ε_d and V values used in the NRG calculations (note that the noninteracting results depend on $-\varepsilon_d/\Gamma$, which labels the upper horizontal axes in panel (b) and its inset). Following the spectral weight curves for peaks P_0 (green squares) and P_1 (red right triangles), in Fig. 5(a), we see that, when U/Γ decreases from 12 to 0.5, the spectral weight of P_0 is almost all transferred to P_1 (although part of the spectral weight of P_0 is also transferred to the continuum and then, with further decrease of U/Γ , to peak P_1). In the interval $0.5 \geq U/\Gamma \geq 0.001$, P_1 quickly acquires spectral weight from inside the continuum, reaching $\approx \frac{2}{3}$ for very small values of U/Γ , as expected. The inset in Fig. 5(a) shows the spectral weight of P_1 in a log scale to emphasize the formation of a $\frac{2}{3}$ plateau as $U \rightarrow 0$.

Figure 5(b) shows the evolution of the position of P_0 (red right triangle) and P_1 (green squares), measured in relation to the bottom of the band. Their variation in position is contrasted to that of the noninteracting bound state (blue circles). Starting from $U/\Gamma = 12$, P_1 (green squares) moves away from the bottom of the band as U/Γ decreases, until, at $U/\Gamma \approx 1$, it reverses course and starts to approach the bottom of the band again. The position of P_1 , the dominant peak for small values of U , progressively approaches the position of the bound state, until they coincide for the two smallest values of U , as emphasized in the inset. Peak P_0 , on the other hand, monotonically approaches the bottom of the band as U/Γ decreases, initially linearly, but then, around the same region where P_1 reverses course, starts to show a faster rate of approach to the bottom of the band as a function

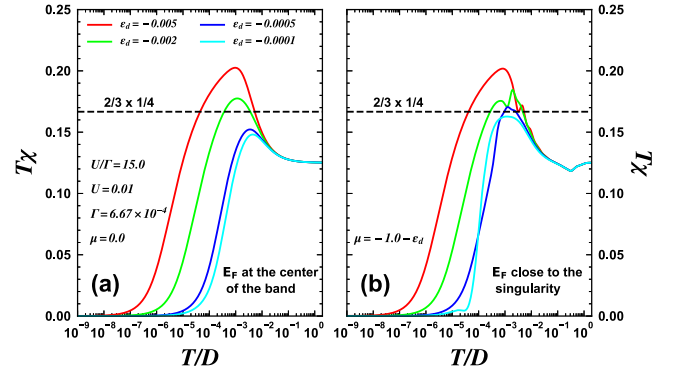


FIG. 6. Impurity magnetic susceptibility χ (as a function of temperature, in units of D , half bandwidth), for some of the ε_d values in Fig. 2(d). (a) The Fermi energy is fixed at the center of the band and, as ε_d gradually increases, the system moves into the intermediate valence regime. Note that, for $\varepsilon_d = -0.005$, the system is in the particle-hole-symmetric (PHS) point. (b) Same as in (a) but now the chemical potential is such that ε_d remains fixed at the singularity, and it is the Fermi energy that moves closer to the bottom of the band; thus, $\mu = -1.0 - \varepsilon_d$. The values of Γ and U are the same as in Fig. 2 for all calculations.

of U/Γ . Note that, to simplify the presentation, even after P_0 split into two peaks, we are considering it a single peak and taking a point halfway between the split peaks as the position of P_0 .

Finally, the results for the position of P_1 [red right triangles in panel (b)] can be interpreted in the following way. As U decreases at fixed Γ , the Fermi energy approaches the bottom of the band since $\varepsilon_d = -U/2$ is at the singularity. Since the Kondo peak becomes broader (as U/Γ decreases), P_1 is initially slowly forced away from the bottom of the band. However, for very small U values ($U/\Gamma \lesssim 1$), the Fermi energy gets very close to the singularity, and since $\Gamma = \pi \rho_0 V^2$ is fixed, V decreases (since ρ_0 increases), and P_1 , which has become the bound state (check comparison with blue circles curve in the inset), approaches the bottom of the band again (check also ε_b in Fig. 15).

C. Thermodynamic properties: Fractional LM

Figure 6 shows the impurity magnetic susceptibility for four values of ε_d (-0.005 , -0.002 , -0.0005 , and -0.0001). In panel (a), the Fermi energy is fixed at the center of the band ($\mu = 0$), and the system stays in a more standard Kondo regime. In contrast, in panel (b), $\mu = -1.0 - \varepsilon_d$, E_F is located close to the bottom of the band, such that ε_d is at the singularity for all cases. Starting at the PHS point $\varepsilon_d = -0.005$ [red curve, panel (a)], the system progressively moves into the intermediate valence regime as ε_d increases (ε_d approaches the Fermi level). As expected, the broad peak around $T \approx 0.001 \ll U = 0.01$, seen in the red curve, is indicative of the LM fixed point. As ε_d moves closer to the Fermi energy, charge fluctuations become more prominent, suppressing the formation of a LM at the impurity (cyan curve). On panel (b), however, where ε_d is at the singularity, and the Fermi energy progressively approaches it, the picture that emerges is substantially different. Although there is little difference

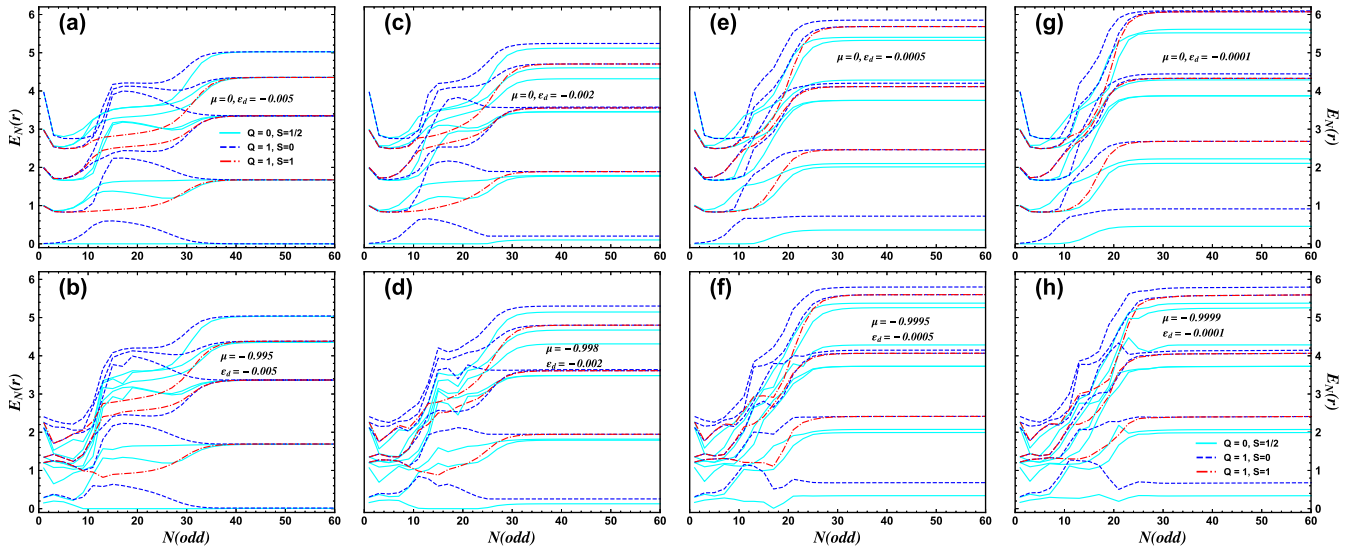


FIG. 7. Numerical renormalization group (NRG) energy flow (for odd values of N) for the same parameters as in Fig. 6. The ε_d values, from left to right, are -0.005 , -0.002 , -0.0005 , and -0.0001 . Top panels correspond to the Fermi energy at the center of the band; lower panels correspond to a Fermi energy close to the bottom of the band (with ε_d at the singularity). Q is the charge in the system, measured in relation to half-filling, while S indicates the total spin (see Ref. [11] for details). The parameter values for U and Γ are the same as in Fig. 6. For these NRG calculations specifically, we have used $\Lambda = 2.5$.

between both panels for $\varepsilon_d = -0.005$ (red curves), once the Fermi energy approaches ε_d , the suppression of the LM peak seems to be arrested in panel (b). The LM peak in χ stays pinned close to the $\frac{2}{3} \times \frac{1}{4}$ value, indicative of the presence of the bound state with spectral weight $Z_b = \frac{2}{3}$ (see the Appendixes), even as ε_d changes by an order of magnitude.

The behavior of χ shown in Fig. 6(b) suggests that the existence of the bound state makes the LM impervious to charge fluctuations. This is corroborated by the NRG energy flows, as shown in Fig. 7, for the same parameters as in Fig. 6. It is well known that the three SIAM fixed points are associated with energy plateaus in the spectra as the number of NRG iterations varies. The free-orbital, LM, and strong-coupling fixed points are successively approached as N increases (which corresponds to a decrease in temperature or energy scale behavior). This can be easily spotted in Fig. 7(a), corresponding to the PHS point, see Refs. [2,11] for comparison. In the upper-row panels (Fermi energy at the center of the band, $\mu = 0$), we see that the plateaus starting at approximately $N = 10$ [Fig. 7(b)] are gradually erased as charge fluctuations increase [panels (c), (e), and (g)]. For example, in Fig. 7(g), the lowest energy state with $Q = 1$ and $S = 0$ (dashed blue curve) transitions directly (around $N = 10$) from a high- to a low-temperature value without going through an intermediate stage. This does not happen for the lower-row panels (E_F close to the bottom of the band). The plateau present in Fig. 7(b) (between $N = 10$ and 30) is still present in panel (h) (although it now finishes at around $N = 20$). This is consistent with the results for a robust Kondo state seen in the impurity magnetic susceptibility in Fig. 6.

For completeness, Fig. 8 shows the impurity entropy as a function of T/D , for the same parameters as in Fig. 6. We note in panel (a) (E_F at the center of the band), for $\varepsilon_d = -0.005$ (red curve), the usual evolution. As temperature decreases, the impurity entropy goes from the free-orbital ($\ln 4$) plateau

to the LM ($\ln 2$) plateau, until it reaches the strong-coupling ($\ln 1$) Kondo limit. Panel (b) shows the corresponding results when the Fermi energy is close to the bottom of the band, with ε_d at the singularity, as in Fig. 6. We notice again a pinning tendency around the LM plateau as ε_d increases, especially for $\varepsilon_d = -0.002$ (green curve), whose oscillation, also observed in the corresponding result in Fig. 6, may be ascribed to the many-body states that appear between the Kondo peak and the singularity [see Fig. 2(b)]. It is important to note the nonuniversal low-temperature behavior of the cyan curve in panel (b), which shows the impurity entropy being negative in the range $10^{-5} \lesssim T/D \lesssim 10^{-4}$. This behavior (which accompanies the nonmonotonic behavior of the cyan curve in $T\chi$, Fig. 6) is reminiscent of the behavior seen in other Kondo problems in the presence of a sharp singularity or

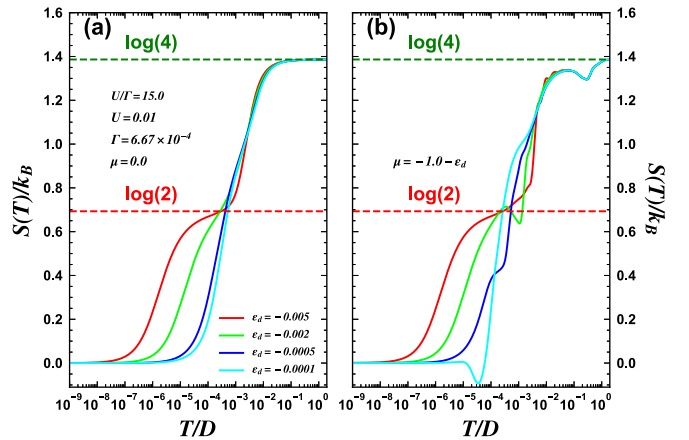


FIG. 8. Impurity entropy (as a function of temperature) for the same parameters as in Fig. 6. See text for discussion of the negative values in the cyan curve in (b).

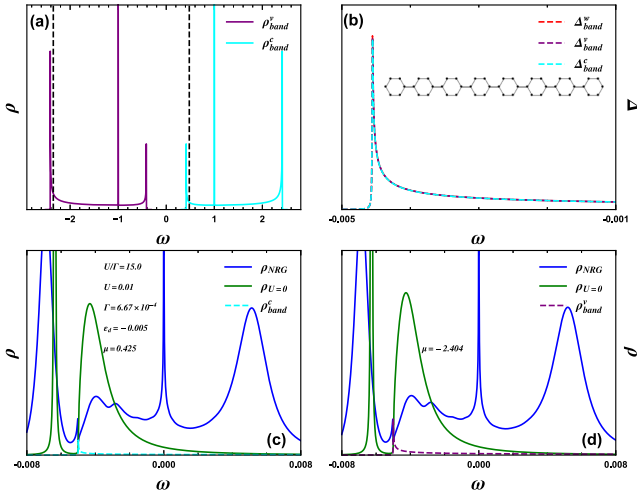


FIG. 9. (a) Armchair graphene nanoribbon made by three carbon rows (3-AGNR) density of states (DOS), showing the very symmetric valence (purple curve) and conduction (cyan) bands. The vertical black dashed lines indicate the approximate position of the Fermi energy for the calculations in (c) and (d). (b) Comparison of the quantum wire singularity (Δ_{band}^w , dashed red curve) with the 3-AGNR valence (Δ_{band}^v , dashed purple) and conduction (Δ_{band}^c , dashed cyan) hybridization functions lower singularities, showing they are identical. The inset shows a sketch of the 3-AGNR system. (c) Impurity DOS (blue curve, ρ_{NRG}) when ε_d is at the singularity at the bottom of the conduction band. The result is very similar to Fig. 2(b), for the quantum wire singularity. (d) Same as in (c) but now ε_d is at the valence band singularity. Also like (c). Parameter values (except for μ) are as in Fig. 2(b).

discontinuity in the DOS [25,26,45] and is clearly most prominent here when the RL is closest to the band singularity.

IV. RESULTS FOR AN AGNR

We now discuss a possible physical implementation of the model NRG results presented in the previous sections. We study the Kondo states associated with band-edge singularities present in the DOS of an AGNR made by three carbon rows (3-AGNR), which is known to be a semiconductor [46,47]. Such nanoribbons can be fabricated from molecular precursors [48], for example, and have been used to study Kondo resonances in experiments [49]. One interesting recent study is that of subgap states in the Kondo regime [50]. Figure 9(a) shows the DOS of an undoped 3-AGNR with symmetric valence and conduction bands. The Fermi energy can, in principle, be gated down until it is close to the bottom singularity of the valence band (leftmost vertical dashed line), or we may gate-dope it with slightly more electrons and bring the Fermi energy just above the bottom singularity of the conduction band (rightmost vertical dashed line). Both cases reproduce the situation studied in the previous sections for the quantum wire. Figure 9(b) compares the ω dependence of these two singularities with that of the quantum wire, showing that they are virtually the same. Notice that panel (b) shows the hybridization function $\Delta(\omega) = \pi V^2 \rho(\omega)$, such that $\Gamma = \pi V^2 \rho(0)$ is the same for all three cases [51]. These results in Fig. 9(b) imply that the NRG results for

the 3-AGNR and the quantum wire should be very similar. Indeed, the finite- U impurity spectral function [same parameters as in Fig. 2(b)], shown in Fig. 9(c), for the conduction band singularity, is quantitatively similar to the quantum wire results in Fig. 2(b). The same occurs for the valence band singularity [Fig. 9(d)] [52].

V. SUMMARY, DISCUSSION, AND CONCLUSIONS

We have analyzed the effect of Van Hove singularities near the Fermi energy and a magnetic impurity on the Kondo effect. Such singularities are present at the band edges of a quantum wire and of different AGNRs. The singularities present at the bottom of the valence and conduction bands of a 3-AGNR result in effective hybridization functions (at fixed Γ) with an $\omega^{-1/2}$ dependence. Thus, the spectral functions of the magnetic impurity are quantitatively similar to those obtained for a quantum wire and provide a convenient physical implementation of our model calculations [48,49,53]. The main results we obtained are as follows. For a noninteracting impurity, we have characterized a Dirac δ bound state below the band minimum, with properties that depend on the near resonance of ε_d with the singularity, and on the coupling of the impurity to the band. As expected, the larger the coupling and the closer ε_d is to the singularity, the larger the spectral weight Z_b of the bound state and the farther it is below the band minimum. The spectral weight Z_b is vanishingly small if ε_d is not close to the singularity, while it quickly increases as it approaches, reaching the value $Z_b = \frac{2}{3}$ at resonance, in agreement with previous work [31], where the singularity is due to spin-orbit interaction (SOI). In addition, the impurity level ε_d is slightly renormalized upward due to its interaction with the singularity (see Fig. 15 and Appendix C).

Once the Hubbard U is present, we see several interesting effects. First, starting with the Fermi energy at the PHS point in the middle of the band [Fig. 2(a)] and then moving to the bottom of the band [Fig. 2(b)], at fixed U and Γ , we see that the noninteracting bound state acquires a finite width [40] and moves further away from the bottom of the band; in addition, a discontinuity appears in the impurity DOS at the band edge. Additional structure in the spectral function appears between this discontinuity and the Kondo peak which, aside from acquiring some asymmetry, is barely affected. An analysis of the evolution of the impurity DOS as U decreases, at fixed Γ , from $U/\Gamma = 12$ to 10^{-3} (see Fig. 4) allows us to follow the evolution of these many-body-related features, until the $U/\Gamma = 10^{-3}$ results match perfectly the $U/\Gamma = 0$ results.

An analysis of how the impurity is discharged as ε_d moves closer to the Fermi energy, starting at the PHS point, shows that there is a great difference in the results for ε_d being far from or close to the singularity. We see in Fig. 2(c) that the approach of ε_d to the singularity recharges the impurity, with the effect being more dramatic as it moves into the intermediate valence regime. This unusual behavior is clearly associated with the existence of the bound state. The Kondo temperature T_K [see Fig. 3(a)], for the same set of parameters, suffers a sizable decrease (if in the intermediate valence regime, with E_F at the center of the band) when E_F moves closer to the singularity at the bottom of the band. Both results, on the

occupancy of the impurity and its T_K value, show that the system partially recovers its strong coupling regime properties, i.e., higher occupancy and lower T_K , once the presence of the singularity is felt at the intermediate valence regime. This occurs because of the formation of the bound state.

In addition, the magnetic susceptibility shows that, for Fermi energy near the bottom of the band and in the intermediate valence regime, the LM fixed point is more resilient, as the impurity suppresses charge fluctuations. Figure 6(b) shows that the LM plateau is somewhat restored around the $\frac{2}{3} \times \frac{1}{4}$ value, indicating the influence of the bound state. This evolution is corroborated by an analysis of the NRG energy flow, shown in Fig. 7, as well as the impurity entropy (Fig. 8).

ACKNOWLEDGMENTS

We thank A. Agarwala and V. B. Shenoy for illuminating exchanges at the beginning of this work, and discussions with E. Vernek, N. Sandler, and G. Diniz. P.A.A. thanks the Brazilian funding agency CAPES for financial support. M.S.F. acknowledges financial support from the National Council for Scientific and Technological Development (CNPq), Grant No. 311980/2021-0, and from the Foundation for Support of Research in the State of Rio de Janeiro (FAPERJ), Processes No. 210 355/2018 and No. E-26/211.605/2021. S.E.U. acknowledges support from the U.S. Department of Energy, Office of Basic Energy Sciences, Materials Science and Engineering Division. G.B.M. acknowledges financial support from CNPq, Processes No. 424711/2018-4, No. 305150/2017-0, and No. 210355/2018.

APPENDIX A: RL IN THE BAND CONTINUUM

We wish to understand how the proximity of a RL (an impurity with $U = 0$) to the singularity at the bottom of the 1D band affects the RL spectral function. We show that the main effect of the singularity is the formation of a bound state out of the continuum, and then we analyze its properties.

We note that Ref. [31] discusses a bound state out of the continuum in three dimensions (3D). There, however, it is necessary to add SOI, while we show that this is not the case in 1D. Thus, we add SOI to the Hamiltonian presented in the main text, Eq. (1), by rewriting it as

$$H_{\text{wire}} = \sum_k \Psi_k^\dagger \mathcal{H}_{\text{wire}}(k) \Psi_k, \quad (\text{A1})$$

where $\Psi_k^\dagger = (c_{k\uparrow}^\dagger, c_{k\downarrow}^\dagger)$, $c_{k\sigma}^\dagger$ creates an electron with wave vector k and spin $\sigma = \uparrow, \downarrow$, and $\mathcal{H}_{\text{wire}}(k)$ is given by

$$\mathcal{H}_{\text{wire}}(k) = (-2t \cos k - \mu)\sigma_0 + (\beta\sigma_x + \alpha\sigma_y)2 \sin k, \quad (\text{A2})$$

where β and α are the Dresselhaus [54] and Rashba [55] SOIs, respectively, while σ_x and σ_y are spin-Pauli matrices, and σ_0 is the 2×2 identity matrix. It can be shown [56] that the energy dispersion associated with this Hamiltonian may be written as

$$\varepsilon_{k\sigma} = -2\sqrt{t^2 + |\gamma|^2} \cos(k - \sigma\varphi) - \mu, \quad (\text{A3})$$

where $\gamma = \beta + i\alpha$, $\varphi = \tan^{-1}(|\gamma|/t)$, and $\sigma = \pm$. The band structure and the DOS for this Hamiltonian are studied in the next Appendix.

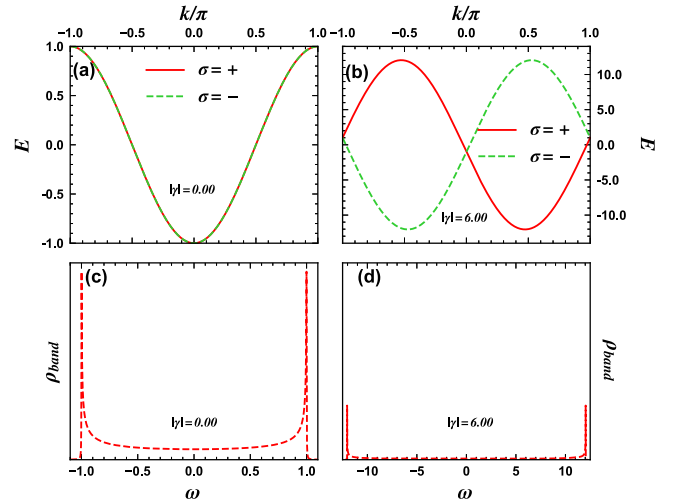


FIG. 10. Band structure for (a) $|\gamma| = 0.0$ and (b) $|\gamma| = 6.0$. Corresponding band density of states (DOS) for the same values of $|\gamma|$, in (c) and (d), respectively. Notice how the singularity for $|\gamma| = 6.0$ in (d) carries a considerably smaller spectral weight than the corresponding singularity for $|\gamma| = 0.0$ in (c). Note that the range in the vertical axes in (c) and (d) are the same, with the integral of ρ_{band} equal to 1 in both cases.

APPENDIX B: BAND STRUCTURE AND SPECTRAL FUNCTION IN 1D WITH SOI

In this Appendix, we show that the inclusion of SOI in 1D (which already has a singularity at the bottom of the band without SOI) decreases the spectral weight of the bound state. Figure 10 shows the band structure in panels (a) ($|\gamma| = 0.0$) and (b) ($|\gamma| = 6.0$), with the corresponding DOS in panels (c) ($|\gamma| = 0.0$) and (d) ($|\gamma| = 6.0$). It is clear that SOI decreases the spectral weight carried by the singularity at the bottom of the band. This happens because a finite SOI increases the bandwidth [compare the range in the horizontal axes in Figs. 10(c) and 10(d)].

We show next that this implies a loss of spectral weight of the bound state associated with the singularity.

We calculate the RL Green's function $\hat{G}_{\text{imp}}(\omega)$, given by

$$\hat{G}_{\text{imp}}(\omega) = [(\omega - \varepsilon_d)\sigma_0 - \hat{\Sigma}^{(0)}(\omega) + i\eta]^{-1}, \quad (\text{B1})$$

where $\hat{\Sigma}^{(0)}(\omega) = \sum_k \hat{V} \hat{G}_{\text{wire}}(k, \omega) \hat{V}^\dagger$ is the hybridization self-energy, with $\hat{V} = V\sigma_0$, $\hat{G}_{\text{wire}}(k, \omega) = [\omega\sigma_0 - \mathcal{H}_{\text{wire}}(k)]^{-1}$ is the quantum wire Green's function, while V is defined right after Eq. (3) in the main text. The RL spectral function, i.e., its DOS, is calculated through (notation as in the main text) $\rho_{U=0}(\omega) = -\frac{1}{\pi} \text{Im Tr } \hat{G}_{\text{imp}}(\omega)$.

A comparison of both the 1D lattice DOS (red curves) and the RL DOS (green curves) is shown in Fig. 11 for $|\gamma| = 0.0$ and $|\gamma| = 1.0$, panels (a) and (b), respectively, where we have set $\varepsilon_d = \omega_{\text{sing}} + \delta$ (where $\delta = 0.05$, and ω_{sing} is the energy at the bottom of the band, with the band being symmetric around $\omega = 0.0$), and $V = 0.25$. A comparison of the RL DOS in both panels shows that a finite SOI decreases the spectral weight of the bound state [thus, the area of the DOS inside the continuum in panel (b) is clearly larger than in panel (a)]. This is further detailed in what follows.

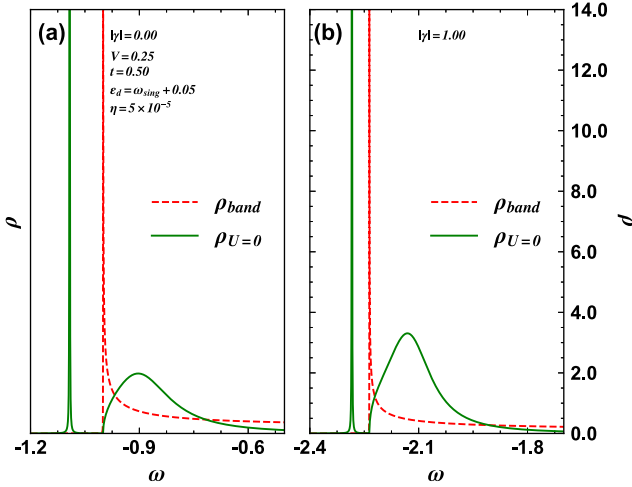


FIG. 11. Band density of states (DOS) ρ_{band} (red dashed curves) and the resonant level (RL) DOS $\rho_{U=0}$ (green curves) for (a) $|\gamma| = 0.0$ and (b) $|\gamma| = 1.0$. The RL orbital energy $\varepsilon_d = \omega_{\text{sing}} + \delta$ is placed at $\delta = 0.05$ above the bottom of the band ω_{sing} , in both cases. In (a), $Z_b = 0.554$, while in (b), $Z_b = 0.415$, showing that the increase of spin-orbit interaction (SOI) makes the bound state less bound and with a weaker spectral weight Z_b . See text for a definition of Z_b .

In Fig. 12, we show results for Z_b , which is defined as

$$Z_b = \int_{-\infty}^{\omega_{\text{sing}}} \rho_{U=0}(\omega) d\omega, \quad (\text{B2})$$

for the interval $0.0 \leq |\gamma| \leq 0.5$, where ω_{sing} is the position of the singularity. It clearly shows that Z_b decreases monotonically with $|\gamma|$. This can be understood by analyzing the ρ_{band} results in Fig. 10, where we can easily see that, for $|\gamma| = 6.0$, there is considerably less spectral weight at the bottom of the band than for $|\gamma| = 0$. Indeed, integrating ρ_{band} from ω_{sing} to $\omega_{\text{sing}} + 0.05$ we obtain ≈ 0.09 for $|\gamma| = 0$ and 0.04 for $|\gamma| = 6.0$. Thus, one expects that the RL will be less affected by the singularity for finite SOI. Again, this occurs because a finite SOI increases the bandwidth.

We have established that the presence of SOI in 1D weakens both the band-edge singularity and the resulting bound

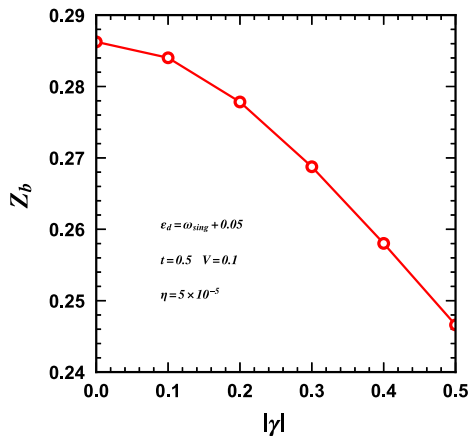


FIG. 12. Variation of the bound state spectral weight Z_b with $|\gamma|$ for $V = 0.1$.

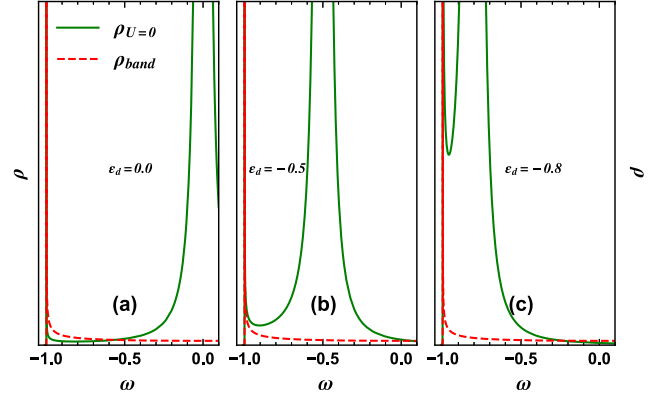


FIG. 13. Resonant level (RL) density of states (DOS) $\rho_{U=0}$ (green curve) for three different positions of the RL: (a) $\varepsilon_d = 0.0$, (b) $\varepsilon_d = -0.5$, and (c) $\varepsilon_d = -0.8$. Notice the large increase of the spectral weight of the peak at the band singularity (red curve) as ε_d approaches the bottom of the band. $V = 0.15$ in all panels.

state. This is in contrast to the 3D system in Ref. [31] that requires SOI to create a singular DOS. In what follows, we analyze the properties of the 1D system without SOI.

APPENDIX C: BOUND STATE PROPERTIES

1. Bound state and coupling to the band

First, we find that, no matter what the energy of the RL is in relation to the singularity, there is always a bound state located either at the singularity or below it [44]. The latter occurs when the coupling of the RL to the band is strong or if the RL is close to the singularity. In Fig. 13, we show the RL DOS $\rho_{U=0}$ for three different positions of the RL in relation to the bottom of the band. In panel (a), the RL is located at the center of the band $\varepsilon_d = 0$, and the singularity is at $\omega = -1.0$. We notice a vanishingly narrow DOS peak at the singularity. In panel (b), the RL is located at $\varepsilon_d = -0.5$, midway between the center of the band and the singularity. The DOS peak at the singularity has increased considerably. Finally, when the RL is just 0.2 above the singularity, $\varepsilon_d = -0.8$, the bound state spectral weight at the singularity has increased drastically. If the coupling increases and/or the RL approaches the singularity even more, the bound state detaches from the band continuum and moves to lower energies, as shown below.

Figure 14(a) shows the RL DOS as we vary its coupling to the band in the range $0.005 \leq V \leq 0.2$, while keeping $\varepsilon_d = \omega_{\text{sing}} + 0.05$. For the smallest $V = 0.005$ (green curve), a bound state at the singularity is not visible (vanishingly small spectral weight). For $V = 0.05$ (blue curve), a very sharp peak at the singularity is already visible (with $Z_b = 0.044$), while for $V = 0.1$ (cyan curve), the bound state has detached from the bottom of the band and moved to lower energies. Its spectral weight has also increased to $Z_b = 0.1566$. This trend continues as V increases. Figure 14(b) shows the Z_b increase with V , reaching more than half of the total spectral weight for $V = 0.25$.

Now we analyze the data in Fig. 14 in more detail. Figure 15 shows how the splitting of the RL ε_d (green circles)

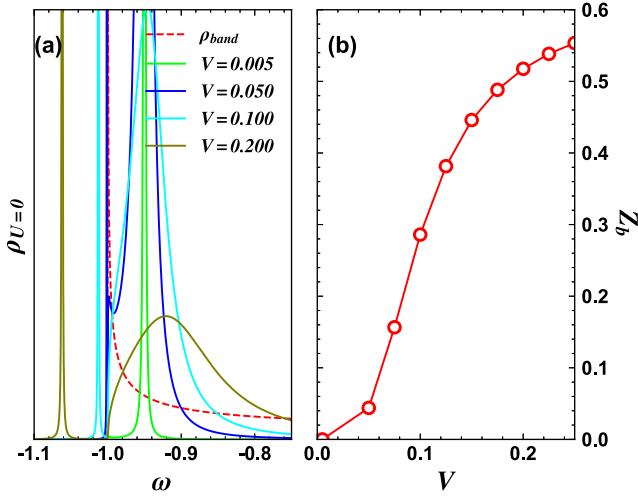


FIG. 14. (a) Variation of the resonant level (RL) density of states (DOS) $\rho_{U=0}$ with the coupling to the band in the interval $0.005 \leq V \leq 0.2$, for $|\gamma| = 0.0$ and $\delta = 0.05$. (b) The variation of Z_b for $0.01 \leq V \leq 0.25$.

into two parts—one, a renormalized peak ε_d^r (blue up triangles) inside the continuum, and the bound state ε_b (magenta down triangles), below the bottom of the band—progresses as one increases V . The red squares mark the bottom of the band.

2. Bound state and distance to singularity

Now we analyze how the bound state varies as we move the RL ε_d closer to the singularity. We set $\varepsilon_d = \omega_{sing} + \delta$, where ω_{sing} marks the bottom of the band, and vary $0.0 \leq \delta \leq 0.04$

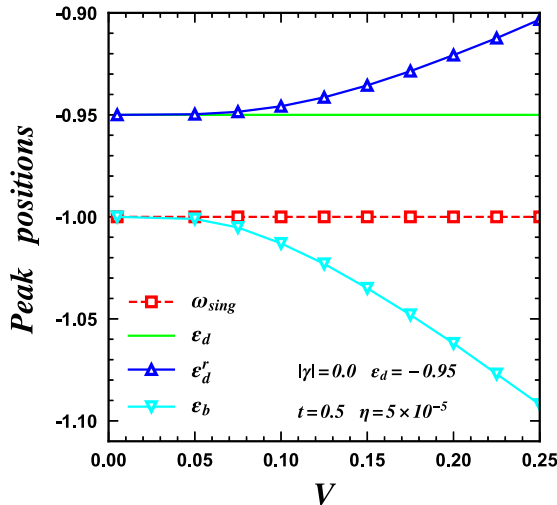


FIG. 15. Analysis of the formation of the bound state in the resonant level (RL) spectral function $\rho_{U=0}$, as a function of V [obtained from the results in Fig. 14(a)]. Red curve shows the bottom of the band (position of the singularity), the green curve shows the position of ε_d , the blue curve shows ε_d^r , the renormalized position of the RL orbital energy, while the cyan curve shows the position of the bound state ε_b .

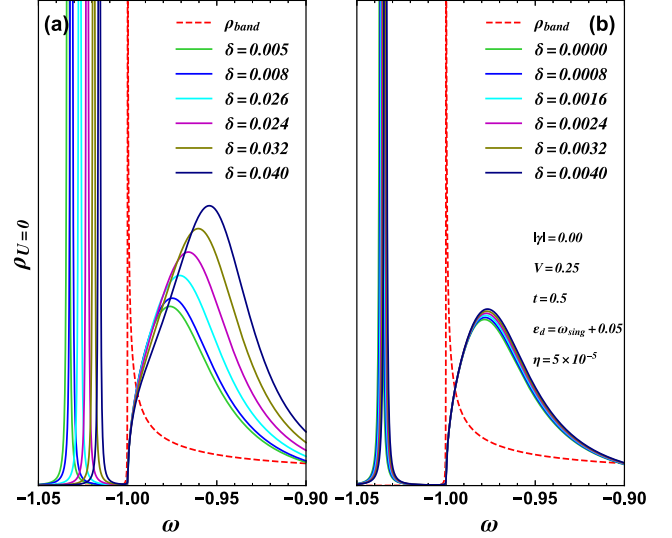


FIG. 16. Variation of $\rho_{U=0}$ with δ (ε_d offset from the bottom of the band) for two different intervals: (a) $0.005 \leq \delta \leq 0.04$ and (b) $0.0005 \leq \delta \leq 0.004$. (a) results show that, starting from $\delta = 0.08$ (dark blue curve), up to $\delta = 0.016$ (blue curve), changes in Z_b and peak positions are considerable, while (b) results show that further approaching ε_d from the bottom of the band ($\delta \leq 0.01$) has limited effects. Results obtained for $|\gamma| = 0.0$ and $V = 0.25$.

(we fix $V = 0.1$). The results are shown in Figs. 16(a) and 16(b). Once ε_d approaches ω_{sing} (δ tends to zero), the variation is very small, i.e., ε_b and Z_b tend to a fixed value.

The variation of Z_b with δ may be seen in Fig. 17. We see that $\delta \rightarrow 0.0$ implies $Z_b \rightarrow \frac{2}{3}$, in agreement with the results obtained in Ref. [31]. This shows the very interesting phenomenon that the $Z_b = \frac{2}{3}$ result does not depend on the details of the band, such as spatial dimensionality (3D vs 1D) and

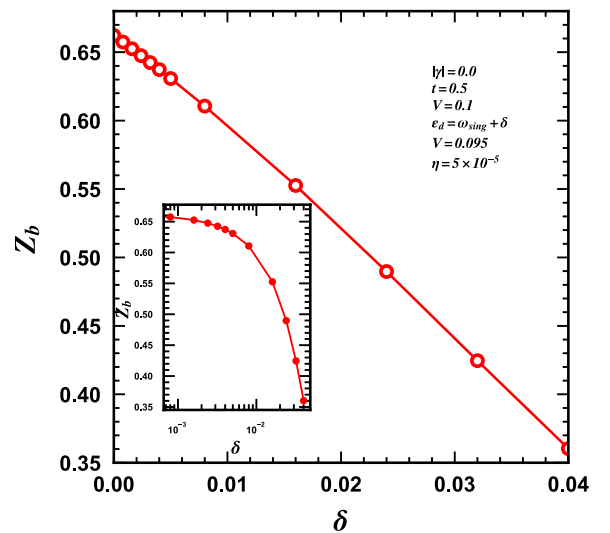


FIG. 17. Variation of the bound state spectral weight Z_b as a function of δ in the interval $0.001 \leq \delta \leq 0.08$. Results obtained from both panels in Fig. 16. The inset shows the same results but with a log scale in the δ axis, highlighting the approach to the $Z_b = \frac{2}{3}$ value.

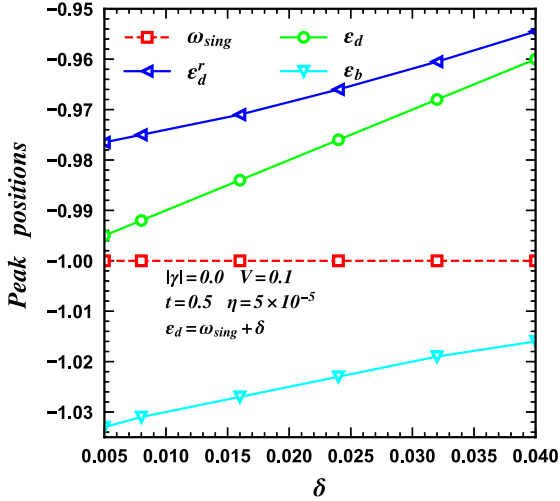


FIG. 18. Similar results as in Fig. 15 but now for the variation of δ . The results shown are just for Fig. 16(a).

presence vs absence of SOI. The inset, with a log scale in the δ axis, emphasizes the gradual approach to the $Z_b = \frac{2}{3}$ value.

Figure 18 shows details of the results in Fig. 16(a), as done in Fig. 15 for the results in Fig. 14(a).

Figure 19 shows what happens when we place ε_d out of the continuum, i.e., $\varepsilon_d = \omega_{\text{sing}} - \delta$ and $0.0 \leq \delta \leq 0.05$, with $V = 0.1$. Panel (b) shows that Z_b takes values above $\frac{2}{3}$, increasing with δ . The DOS inside the continuum, as can be seen in panel (b), tends to accumulate at the bottom of the band as δ increases.

Finally, Fig. 20 shows details of the results in Fig. 19(a).

APPENDIX D: STUDY OF THE IMPURITY SPECTRAL FUNCTION

In this section, we follow Ref. [57] and do a step-by-step analysis of the results in Figs. 2 and 4 to show that the NRG

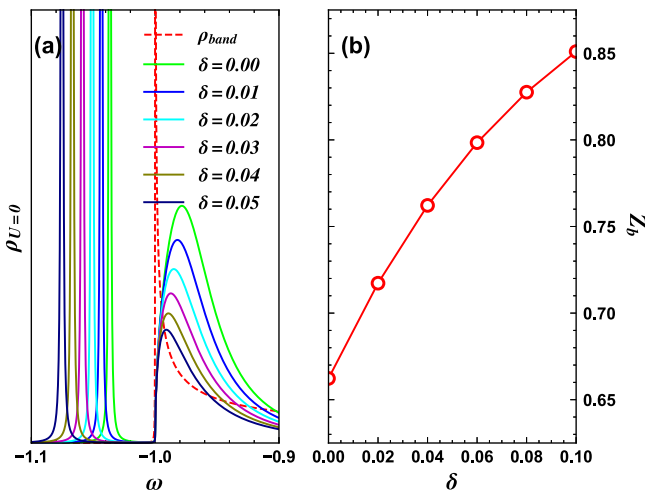


FIG. 19. Similar results as in Fig. 16 but now when the impurity is placed below the bottom of the band (note that $\varepsilon_d = \omega_{\text{sing}} - \delta$) and $V = 0.1$. (a) Results for $\rho_{U=0}$, for $0.0 \leq \delta \leq 0.1$, showing again the peak splitting. (b) Spectral weight Z_b of the bound state, now $> \frac{2}{3}$.

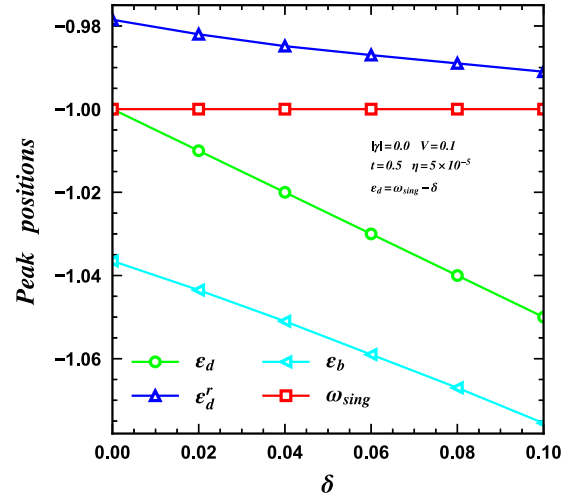


FIG. 20. Similar results as in Fig. 18 but now ε_d (green curve) is placed below the bottom of the band. Larger peak separations are obtained this way.

spectral function features discussed in Secs. III A and III B are not numerical artifacts. There are quite a few aspects that should be considered to root out NRG artifacts in the impurity spectral function ρ_{NRG} . According to Žitko and Pruschke [57], overbroadening effects reduce energy resolution at higher energies and wash out spectral features with small spectral weight (like P_1 , in Figs. 2 and 4, for the larger values of U/Γ). The so-called interleaved method (or z averaging) [36] allows for the use of narrower broadening functions, mitigating overbroadening and removing oscillatory features in the impurity spectral function. The method consists of performing several (N_z) NRG calculations for different logarithmic discretization meshes and then taking their average to obtain the final impurity spectral function. However, one must check that convergence has been attained before trying to root out artifacts. Figure 21 shows the evolution of ρ_{NRG} with increasing N_z in the interval $4 \leq N_z \leq 128$. It is clear that $N_z = 4$ (green curve) is not nearly enough; however, for $N_z \geq 16$, ρ_{NRG} has converged. It is interesting to note that P_1 is the last feature to converge. Indeed, the largest difference (which occurs around P_1 , as shown in the inset) between $N_z = 16$ and 8 is $\approx 4.1\%$, while it is $\approx 1.5\%$ for the difference between $N_z = 32$ and 16. This value falls to $\approx 0.4\%$ for $N_z = 64$ (in relation to 32), and to $\approx 0.08\%$ for $N_z = 128$ (in relation to 64). Thus, for the purpose of exposing numerical artifacts [57] (see next step), all spectral function features are well converged for $N_z = 32$.

The next step, once N_z convergence of all ρ_{NRG} features has been ensured, is to analyze its dependence with Λ (discretization parameter). Indeed, artifacts will shift (and change form) substantially when Λ varies, while real features will change very little [57]. Usually, the detection of artifacts is more effectively done when one studies the approach to the continuum limit ($\Lambda \rightarrow 1$). Thus, we decreased the discretization parameter below the standard $\Lambda = 2$ value (down to 1.6). Figure 22 shows ρ_{NRG} results for the same parameters as in Fig. 2(b) (except that now $N_z = 32$), for the interval $1.6 \leq \Lambda \leq 2$ (varying in steps of 0.1). It is clear that peaks P_0 and P_1 , which were discussed in detail in Sec. III B, suffer marginal changes, indicating that they are not numerical artifacts.

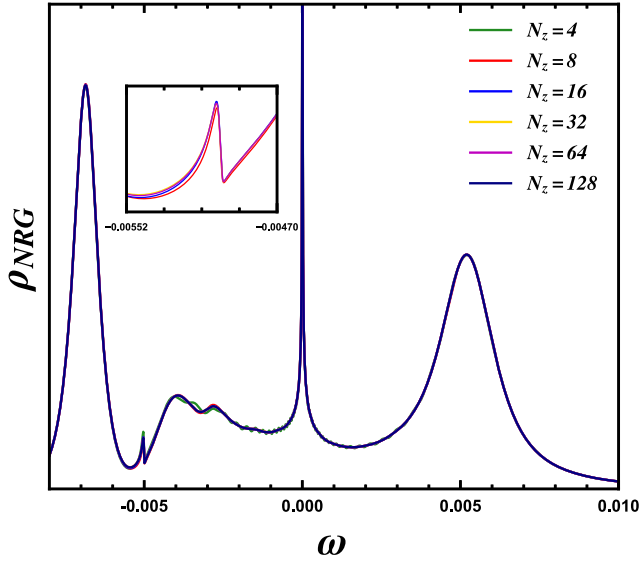


FIG. 21. Analysis of the ρ_{NRG} dependence on N_z (interleaving parameter [57]) for the results in Fig. 2(b), in the interval $4 \leq N_z \leq 128$. The inset shows a zoom in the region where the curves (except for $N_z = 4$) vary the most (around P_1). Taking the peak-height change as a measure of the overall variation in this region, we obtain that the variation between $N_z = 16$ and 8, $N_z = 32$ and 16, $N_z = 64$ and 32, and $N_z = 128$ and 64 is 4.1, 1.5, 0.4, and 0.08%, respectively. Thus, for the purpose of presentation, the results are already well converged for $N_z = 16$ (value used in this paper). As to exposing numerical artifacts, good convergence has been achieved for $N_z = 32$ (see text).

One last step consists of applying the so-called self-energy trick [58] (dubbed Σ - t , for short, in Fig. 23), which is a very efficient method to reduce overbroadening effects [57]. This trick consists of calculating the impurity self-energy as the ratio of two correlation functions and then using it to obtain the impurity Green's function, whose imaginary part is

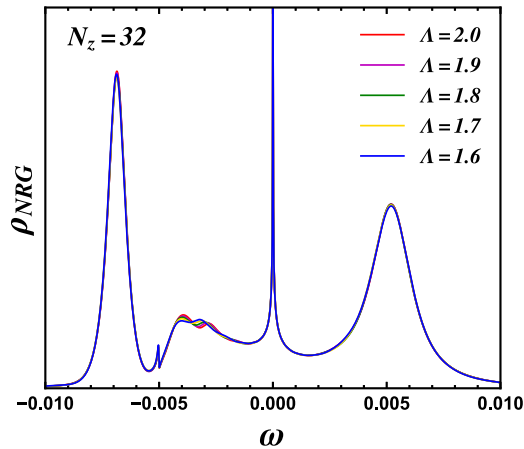


FIG. 22. Analysis of the Δ dependence of the ρ_{NRG} results in Fig. 2(b) in the interval $1.6 \leq \Delta \leq 2$. As shown in Ref. [57], numerical renormalization group (NRG) discretization artifacts should shift position and change form significantly with decreasing Δ . Note that we use the well-converged $N_z = 32$ results for this analysis.

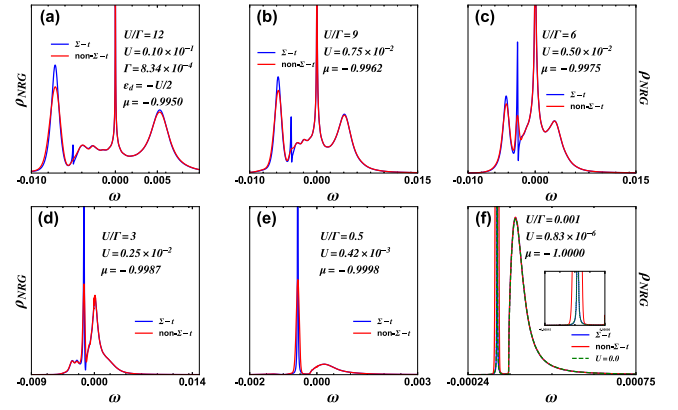


FIG. 23. Reproduction of the results in Fig. 4, comparing the impurity spectral function ρ_{NRG} calculated using the so-called self-energy trick [58] (blue curves) with the results obtained without its use (red curves). The inset in (f) zooms in on the bound state, showing that the self-energy trick removes the overbroadening and produces the exact result (dashed green curve).

proportional to the impurity spectral function. It is important to remark that all our spectral function results in this paper were obtained by using Σ - t . In Fig. 23, we compare our results for Fig. 4 (obtained through Σ - t , blue curves) with the results obtained without the use of Σ - t (red curves). There are some interesting points to stress. First, in all panels, the use of Σ - t results in the narrowing of some features, most notably of P_1 , mainly in panels (a) and (b), where P_1 is barely noticeable without Σ - t [especially in panel (a)]. In addition, we want to call special attention to the result in panel (f), where the use of Σ - t (blue curve) has narrowed the non- Σ - t result (red curve) almost perfectly into the exact noninteracting ($U = 0$) result (dashed green curve). This is emphasized in the inset of panel (f). Since there is no reason for the accuracy of the Σ - t spectral function to be reduced for finite U [58], we can have confidence in the accuracy of the spectral function results presented in Figs. 2 and 4.

The NRG package used here (NRG Ljubljana [35]) has the so-called patching procedure [59] fully implemented, and it was used in all spectral function calculations done here. It is well known that the NRG is an iterative procedure which

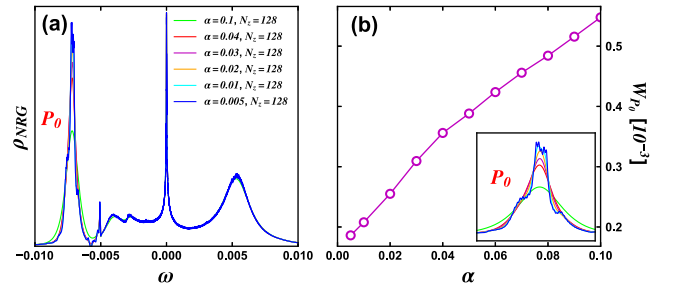


FIG. 24. (a) Variation of ρ_{NRG} —same parameters as in Fig. 4(a) but now for $N_z = 128$ instead of 16—with the numerical renormalization group (NRG) broadening parameter $0.005 \leq \alpha \leq 0.1$. (b) Half-width at half-height W_{P_0} of the P_0 peak in (a) as a function of α . The inset shows a zoom of P_0 .

solves consecutive so-called Wilson chains with increasing sizes N . The energy window being analyzed, at each specific stage of the iterative procedure, logarithmically approaches the ground-state region of the spectra for two consecutive iterations. One must carefully join (patch) the spectral information acquired at iterations $N + 2$ and N . This procedure results in a smooth spectral function across energy windows at different energy scales.

Finally, to analyze if the finite width of P_0 , observed in Fig. 4, is caused by NRG overbroadening, we present, in Fig. 24(a), ρ_{NRG} for the same parameters as in Fig. 4(a) but now for $N_z = 128$ (instead of 16) and varying values of the

broadening NRG parameter $0.005 \leq \alpha \leq 0.1$ [60]. As shown in Fig. 21, the result for $\alpha = 0.1$ (green curve) [same α as used in Fig. 4(a)] changes very little when we increase N_z , in this case, from $N_z = 16$ [Fig. 4(a), blue curve] to $N_z = 128$ [Fig. 24(a), green curve]. For decreasing α values, we see that the largest changes in ρ_{NRG} occur for P_0 [a zoom of P_0 is shown in the inset in Fig. 24(b)]. As shown in panel (b), the P_0 half-width at half-height, denoted W_{P_0} , decreases by 67% (from 5.5×10^{-4} to 1.8×10^{-4}), while α decreases 20 times (from 0.1 to 0.05). However, one cannot rule out the possibility that the peak width will extrapolate to zero. Thus, NRG cannot conclusively resolve this issue.

-
- [1] A. C. Hewson, *The Kondo Problem to Heavy Fermions*, Cambridge Studies in Magnetism (Cambridge University Press, Cambridge, 1993).
- [2] H. R. Krishna-murthy, J. W. Wilkins, and K. G. Wilson, Renormalization-group approach to the Anderson model of dilute magnetic alloys. I. Static properties for the symmetric case, *Phys. Rev. B* **21**, 1003 (1980).
- [3] V. Madhavan, W. Chen, T. Jamneala, M. Crommie, and N. Wingreen, Tunneling into a single magnetic atom: Spectroscopic evidence of the Kondo resonance, *Science* **280**, 567 (1998).
- [4] D. Goldhaber-Gordon, H. Shtrikman, D. Mahalu, D. Abusch-Magder, U. Meirav, and M. Kastner, Kondo effect in a single-electron transistor, *Nature (London)* **391**, 156 (1998).
- [5] P. Coleman, *Introduction to Many-Body Physics* (Cambridge University Press, Cambridge, 2015).
- [6] P. W. Anderson, Localized magnetic states in metals, *Phys. Rev.* **124**, 41 (1961).
- [7] J. R. Schrieffer and P. A. Wolff, Relation between the Anderson and Kondo Hamiltonians, *Phys. Rev.* **149**, 491 (1966).
- [8] J. Kondo, Resistance minimum in dilute magnetic alloys, *Prog. Theor. Phys.* **32**, 37 (1964).
- [9] K. G. Wilson, The renormalization group: Critical phenomena and the Kondo problem, *Rev. Mod. Phys.* **47**, 773 (1975).
- [10] K. G. Wilson, The renormalization group and critical phenomena, *Rev. Mod. Phys.* **55**, 583 (1983).
- [11] R. Bulla, T. A. Costi, and T. Pruschke, Numerical renormalization group method for quantum impurity systems, *Rev. Mod. Phys.* **80**, 395 (2008).
- [12] M. Vojta and R. Bulla, A fractional-spin phase in the power-law Kondo model, *Eur. Phys. J. B* **28**, 283 (2002).
- [13] D. Withoff and E. Fradkin, Phase transitions in gapless Fermi systems with magnetic impurities, *Phys. Rev. Lett.* **64**, 1835 (1990).
- [14] L. S. Borkowski and P. J. Hirschfeld, Kondo effect in gapless superconductors, *Phys. Rev. B* **46**, 9274 (1992).
- [15] K. Chen and C. Jayaprakash, The Kondo effect in pseudo-gap Fermi systems: A renormalization group study, *J. Phys.: Condens. Matter* **7**, L491 (1995).
- [16] K. Ingersent, Behavior of magnetic impurities in gapless Fermi systems, *Phys. Rev. B* **54**, 11936 (1996).
- [17] R. Bulla, T. Pruschke, and A. C. Hewson, Anderson impurity in pseudo-gap Fermi systems, *J. Phys.: Condens. Matter* **9**, 10463 (1997).
- [18] C. Gonzalez-Buxton and K. Ingersent, Renormalization-group study of Anderson and Kondo impurities in gapless Fermi systems, *Phys. Rev. B* **57**, 14254 (1998).
- [19] R. Bulla, M. T. Glossop, D. E. Logan, and T. Pruschke, The soft-gap Anderson model: Comparison of renormalization group and local moment approaches, *J. Phys.: Condens. Matter* **12**, 4899 (2000).
- [20] K. Ingersent and Q. Si, Critical local-moment fluctuations, anomalous exponents, and ω/T scaling in the Kondo problem with a pseudogap, *Phys. Rev. Lett.* **89**, 076403 (2002).
- [21] L. G. G. V. Dias da Silva, N. Sandler, P. Simon, K. Ingersent, and S. E. Ulloa, Tunable pseudogap Kondo effect and quantum phase transitions in Aharonov-Bohm interferometers, *Phys. Rev. Lett.* **102**, 166806 (2009).
- [22] R. Žitko, J. Bonča, and T. Pruschke, Van Hove singularities in the paramagnetic phase of the Hubbard model: DMFT study, *Phys. Rev. B* **80**, 245112 (2009).
- [23] A. K. Mitchell and L. Fritz, Kondo effect with diverging hybridization: Possible realization in graphene with vacancies, *Phys. Rev. B* **88**, 075104 (2013).
- [24] A. K. Mitchell, M. Vojta, R. Bulla, and L. Fritz, Quantum phase transitions and thermodynamics of the power-law Kondo model, *Phys. Rev. B* **88**, 195119 (2013).
- [25] A. Zhuravlev, Negative impurity magnetic susceptibility and heat capacity in a Kondo model with narrow peaks in the local density of electron states, *Phys. Metals Metallogr.* **108**, 107 (2009).
- [26] A. K. Zhuravlev and V. Y. Irkhin, Kondo effect in the presence of van Hove singularities: A numerical renormalization group study, *Phys. Rev. B* **84**, 245111 (2011).
- [27] R. Žitko and J. Bonča, Kondo effect in the presence of Rashba spin-orbit interaction, *Phys. Rev. B* **84**, 193411 (2011).
- [28] Y. E. Shchadilova, M. Vojta, and M. Haque, Single-impurity Kondo physics at extreme particle-hole asymmetry, *Phys. Rev. B* **89**, 104102 (2014).
- [29] R. Žitko and A. Horvat, Kondo effect at low electron density and high particle-hole asymmetry in 1D, 2D, and 3D, *Phys. Rev. B* **94**, 125138 (2016).
- [30] A. Wong, S. E. Ulloa, N. Sandler, and K. Ingersent, Influence of Rashba spin-orbit coupling on the Kondo effect, *Phys. Rev. B* **93**, 075148 (2016).
- [31] A. Agarwala and V. B. Shenoy, Quantum impurities develop fractional local moments in spin-orbit coupled systems, *Phys. Rev. B* **93**, 241111(R) (2016).

- [32] J.-C. Charlier, X. Blase, and S. Roche, Electronic and transport properties of nanotubes, *Rev. Mod. Phys.* **79**, 677 (2007).
- [33] K. Wakabayashi, K. ichi Sasaki, T. Nakanishi, and T. Enoki, Electronic states of graphene nanoribbons and analytical solutions, *Sci. Technol. Adv. Mater.* **11**, 054504 (2010).
- [34] A similar result was obtained in Ref. [31] for a 3D free-electron gas with a very strong SOI. That system shows an SOI-dependent singularity at the bottom of the band. The authors solve the problem in the continuum and use an energy cutoff to handle the divergence. We stress that the 1D lattice model already contains a divergence at the bottom of the band, and there is no need to introduce SOI. The introduction of SOI in the 1D wire weakens the bound state, as shown in the Appendixes.
- [35] R. Žitko, *NRG Ljubljana* (2021).
- [36] V. L. Campo and L. N. Oliveira, Alternative discretization in the numerical renormalization-group method, *Phys. Rev. B* **72**, 104432 (2005).
- [37] W. Hofstetter, Generalized numerical renormalization group for dynamical quantities, *Phys. Rev. Lett.* **85**, 1508 (2000).
- [38] The sign of the chemical potential in Eq. (1) is such that $\mu = 0$ corresponds to half-filling (Fermi energy at the center of the band), and $\mu = -D = -1.0$ corresponds to the Fermi energy at the singularity (at the bottom of the band).
- [39] Note that the spectral weight of the bound state (not shown) for $\mu = 0$ is vanishingly small (see the Appendixes).
- [40] In Appendix D, we were able to show that most of the features present in the impurity spectral function are real. Although suggestive of an actual finite width for the bound state (peak P_0), one cannot ascertain its finite value and independence of calculation parameters.
- [41] See Eq. (B2) for the definition of the bound state spectral weight Z_b .
- [42] T. A. Costi and V. Zlatić, Thermoelectric transport through strongly correlated quantum dots, *Phys. Rev. B* **81**, 235127 (2010).
- [43] Notice that, at the bottom of Fig. 3(a), the system is in an intermediate valence regime, so that a proper Kondo temperature is not well defined. However, as shown in Figs. 6 and 7, the presence of the bound state strongly affects the LM fixed point of the impurity, suppressing its charge fluctuations, forcing it back into the Kondo regime.
- [44] We have checked that the $U = 0$ bound state is a Dirac δ function since its half-width at half-height is exactly η [see Eq. (B1)].
- [45] D. Mastrogiuseppe, A. Wong, K. Ingersent, S. E. Ulloa, and N. Sandler, Kondo effect in graphene with Rashba spin-orbit coupling, *Phys. Rev. B* **90**, 035426 (2014).
- [46] H.-H. Lin, T. Hikihara, H.-T. Jeng, B.-L. Huang, C.-Y. Mou, and X. Hu, Ferromagnetism in armchair graphene nanoribbons, *Phys. Rev. B* **79**, 035405 (2009).
- [47] P. A. Almeida, L. S. Sousa, T. M. Schmidt, and G. B. Martins, Ferromagnetism in armchair graphene nanoribbon heterostructures, *Phys. Rev. B* **105**, 054416 (2022).
- [48] J. Cai, P. Ruffieux, R. Jaafar, M. Bieri, T. Braun, S. Blankenburg, M. Muoth, A. P. Seitsonen, M. Saleh, X. Feng *et al.*, Atomically precise bottom-up fabrication of graphene nanoribbons, *Nature (London)* **466**, 470 (2010).
- [49] Y. Li, A. T. Ngo, A. DiLullo, K. Z. Latt, H. Kersell, B. Fisher, P. Zapol, S. E. Ulloa, and S.-W. Hla, Anomalous Kondo resonance mediated by semiconducting graphene nanoribbons in a molecular heterostructure, *Nat. Commun.* **8**, 946 (2017).
- [50] P. Zalom and M. Žonda, Subgap states spectroscopy in a quantum dot coupled to gapped hosts: Unified picture for superconductor and semiconductor bands, *Phys. Rev. B* **105**, 205412 (2022).
- [51] A calculation for a 5-AGNR shows the same behavior, viz., the bottom singularities for the valence and conduction bands produce identical hybridization functions to the one for the quantum wire.
- [52] An NRG analysis for the case where ε_d is resonant with the very sharp conduction band singularity at $\omega = 1.0$ [see Fig. 9(a)] demands a much more sophisticated discretization procedure (see, for example, Ref. [61]). We leave this problem as a subject for a future work.
- [53] T. Kitao, M. W. A. MacLean, K. Nakata, M. Takayanagi, M. Nagaoka, and T. Uemura, Scalable and precise synthesis of armchair-edge graphene nanoribbon in metal-organic framework, *J. Am. Chem. Soc.* **142**, 5509 (2020).
- [54] G. Dresselhaus, Spin-orbit coupling effects in zinc blende structures, *Phys. Rev.* **100**, 580 (1955).
- [55] Y. A. Bychkov and E. I. Rashba, Oscillatory effects and the magnetic susceptibility of carriers in inversion layers, *J. Phys. C* **17**, 6039 (1984).
- [56] V. Lopes, G. B. Martins, M. A. Manya, and E. Anda, V, Kondo effect under the influence of spin-orbit coupling in a quantum wire, *J. Phys.: Condens. Matter* **32**, 435604 (2020).
- [57] R. Žitko and T. Pruschke, Energy resolution and discretization artifacts in the numerical renormalization group, *Phys. Rev. B* **79**, 085106 (2009).
- [58] R. Bulla, A. C. Hewson, and T. Pruschke, Numerical renormalization group calculations for the self-energy of the impurity Anderson model, *J. Phys.: Condens. Matter* **10**, 8365 (1998).
- [59] R. Bulla, T. A. Costi, and D. Vollhardt, Finite-temperature numerical renormalization group study of the Mott transition, *Phys. Rev. B* **64**, 045103 (2001).
- [60] The Gaussian broadening used η is related to α by $\eta = \alpha|E|$, where E is the pole being broadened.
- [61] R. Žitko, Adaptive logarithmic discretization for numerical renormalization group methods, *Comput. Phys. Commun.* **180**, 1271 (2009).